AGU PUBLICATIONS

Water Resources Research

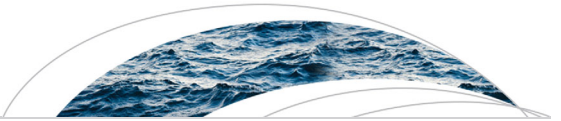

RESEARCH ARTICLE

10.1002/2016WR019524

# Analytical solutions for aquifer thermal energy storage

**Jan Martin Nordbotten**[1,2]

[1]Department of Mathematics, University of Bergen, Bergen, Norway, [2]Department of Civil and Environmental Engineering, Princeton University, Princeton, New Jersey, USA

**Key Points:**
- Closed-form solutions incorporating density and viscosity differences
- Validation of modeling assumption based on field data from 24 analog sites
- Verification across parameter range based on comparisons to numerical simulation

**Correspondence to:**
J. M. Nordbotten,
jan.nordbotten@math.uib.no

**Citation:**
Nordbotten, J. M. (2017), Analytical solutions for aquifer thermal energy storage, *Water Resour. Res.*, *53*, 1354–1368, doi:10.1002/2016WR019524.

Received 17 JUL 2016
Accepted 10 JAN 2017
Accepted article online 13 JAN 2017
Published online 10 FEB 2017

**Abstract** The concept of aquifer thermal energy storage involves injection of water at elevated temperature, and possibly nonambient salinity, into a host aquifer. We consider axisymmetric injection, wherein both the composition and temperature of the injected fluid differ from the fluid in the target aquifer. In this setting, we derive the governing equations within a vertically integrated framework, and show their self-similar structure. We subsequently derive explicit approximate solutions to the self-similar equations for parameter ranges of relevance to thermal energy storage (small density and viscosity differences). The analysis is supported by numerical validation, covering the relevant parameter regime. The resulting comparisons demonstrate the mathematical qualities of the analytical approximations. A study based on field data from analogue sites justifies the assertions regarding the magnitude of the dimensionless parameters used in the analysis.

## 1. Introduction

Intermittent renewable energy sources, such as wind and solar, are an increasing component of the global energy portfolio. The unpredictable and intermittent nature of these renewable energy sources is poorly aligned with consumer demand. As such, energy storage technologies are essential in order to minimize energy losses and bridge periods between surplus production and excess demand.

The subsurface represents an attractive energy storage medium and holds the potential for storing large amounts of energy with minimal footprint on the land surface. Storage mechanisms in the subsurface can be divided into mechanical (pressure), chemical (gas), and thermal.

Thermal energy storage, in the form of aquifer thermal energy storage, is the concept of injection of a hot fluid (typically water) into an aquifer, for recovery of thermal energy at a later stage. This is advantageous in particular when surplus energy is available in the form of heat (either from cooling of industrial processes [*Ueckert et al*., 2016] or from e.g., solar heating), that can be matched to a later energy demand associated with heating (e.g., seasonal heating in variable climates). The technology has been experimentally shown to yield energy recovery factors of around 66-89% [*Molz et al*., 1981; see also *Palmer et al*., 1982; *Perlinger et al*., 1987]. However, a key obstacle with respect to efficient energy recovery lies in the buoyancy and viscosity associated with injection of hot fluids into a relatively colder aquifer – leading to adverse effects in the form of unstable displacement and onset of thermal convection [*Molz et al*., 1983].

Fluid displacement in view of buoyant and viscous effects can be readily modeled within a vertically integrated framework. This concept relies on modeling a two-dimensional domain with vertically integrated fluid content as primary variables (naturally interpreted as the vertical extent of fluid zones), rather than three-dimensional pointwise fluid properties. This approach has been utilized both within groundwater intrusion [*Bear*, 1979], petroleum recovery [*Lake*, 1989] and $CO_2$ storage [*Nordbotten and Celia*, 2012], and has been validated both theoretically [*Yortsos*, 1995; *Nordbotten and Celia*, 2006], numerically [*Court et al*., 2012], experimentally [*Huppert and Woods*, 1995] and through comparison to field data [*Mykkeltvedt and Nordbotten*, 2012]. However, the majority of existing work on vertically integrated models has focused on capturing only the displacement process, without accounting for the thermal front. Notable exceptions include work motivated by heat storage in unconfined systems [*Dudfield and Woods*, 2012] and confined systems with line symmetry [*Rayward-Smith and Woods*, 2011], as well as thermal effects during $CO_2$ storage [*Gasda et al*., 2014].

Herein, we will use the vertically integrated framework to derive equations for the advancement of both the mass front (associated with the displacement of resident aquifer brine with injection fluid), as well as the

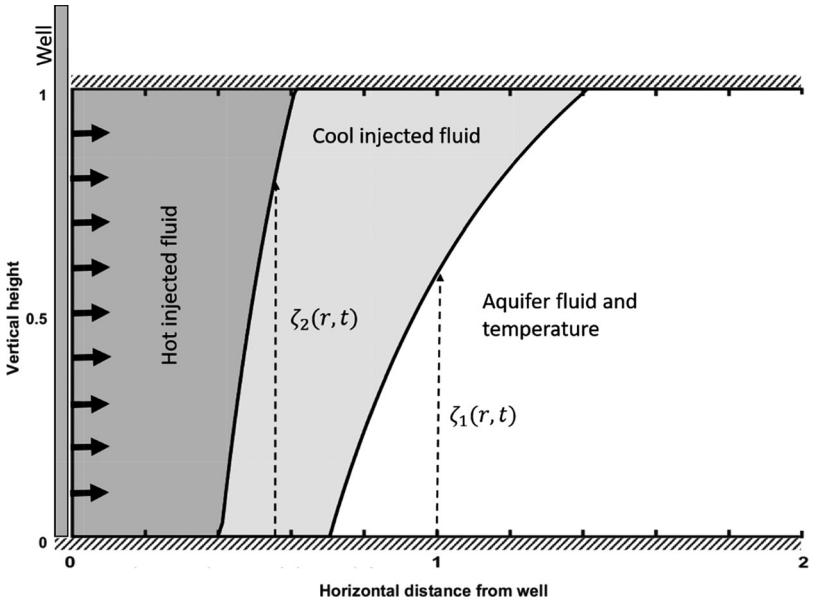


**Figure 1.** Schematic of fluid injection from well (left axis), where the injected fluid is shaded darker gray. As the fluid progresses into the aquifer, thermal and mass fronts develop, indicated by the elevations $\zeta_2$ and $\zeta_1$. Between the fronts, the fluid will be at injected composition but ambient temperature (light gray). The original aquifer fluid is displaced ahead of the fronts (white). In this geometry, the aquifer boundaries (top and bottom) are impermeable, while the horizontal extent continues to infinity.

thermal front. The thermal front will typically advance significantly slower than the mass front due to the thermal capacity of the aquifer rocks. We apply the equations for mass and energy conservation to the problem of fluid injection, and consider a radial geometry within a confined aquifer. With this geometry, the solutions are self-similar in $[length]^2/[\text{time}]$ coordinates [*Barenblatt*, 1996], thus shape of the solution (up to a spatial scaling) is independent of time. Furthermore, we can obtain analytical solutions for the limit of high injection rates (relative to buoyant forces), and also explicit approximate solutions whenever the injection rate is moderately high, coupled with small viscosity differences between the injected and ambient fluids. These are the relevant conditions for thermal energy storage.

We note that the consideration of a radial geometry leads to a fundamentally different structure than that of a linear geometry (as in the case of a horizontal well, or a line of vertical wells). In a radial geometry, the buoyant spreading and advective forces balance, whereas in a linear geometry, the buoyant spreading will gradually become of less importance, and a purely advective analysis is valid at late time [*Huppert and Woods*, 1995; *Hesse et al*., 2007; *Nordbotten and Celia*, 2012]. These considerations are valid for confined aquifers, whereas for an unconfined aquifer, fundamentally more complex analysis is needed due to the a priori unknown total vertical extent of the fluid layers [*Barenblatt*, 1996].

After validating our analytical solutions, we discuss the relevant implications for thermal-viscous instability based on data from 24 analogue injection sites.

## 2. Model for Thermal Injection

In this section, we will present a simplified mathematical model for thermal injection. The model will be based on a vertically integrated formalism [*Lake*, 1989; *Bear*, 1979; *Nordbotten and Celia*, 2012], and account both for solute and heat transport.

When hot fluid is injected into a storage aquifer, in general two fronts will appear, as indicated in Figure 1. Outermost, there will be a front tracking the actual injected fluid, and thus indicating a discontinuity in fluid composition. Closer to the well, there will be a secondary front tracking the thermal front. The thermal front is slower than the compositional front due to the heat capacity of the rock. While this structure can be resolved using fully compositional and thermal equations for flow in porous media [see e.g., *Chen et al*.,

2006]), we will in contrast assume this solution structure a priori, and therefore directly solve for the fronts themselves as our primary variables.

In the interest of simplicity of exposition, we will follow [*Nordbotten and Celia*, 2006] and limit the presentation to horizontal aquifers with uniform thickness, and to incompressible (but variable density) fluids. We will also only consider radial flow from the injection well. These limitations are not fundamental, and the model presented herein can readily be extended in this regard, as has been done for related models [see e.g., *Nordbotten and Celia*, 2012; *Gasda et al*., 2012].

Two key assumptions are required in order to apply the vertically integrated formalism: (A) The time-scales of consideration need to be long enough for fluid segregation to be applicable. This assumption is discussed in detail in the context of $CO_2$ storage in previous works [*Nordbotten and Dahle*, 2011]. (B) The processes under consideration must be advection dominated. In particular, we will herein neglect dispersion, diffusion and heat conduction, all three assumptions being consistent with relatively high injection rates. The horizontal impact of diffusive/conductive spreading scales with the same $[\textit{length}]^2/[\text{time}]$ as the injection process (for a radial geometry), however the vertical impact of diffusive and conductive spreading scales with $[\textit{length}]/[\text{time}]$. Assumption B) may thus be violated at very long time scales, and in order for both assumptions A) and B) to have overlapping applicability, the density difference between the fluids must be sufficiently large compared to the vertical diffusive, dispersive and conductive material properties.

The model development in sections 2.1 and 2.2 mostly summarizes previous work for the mathematically equivalent case of $CO_2$ injection with a secondary drying front [*Nordbotten and Celia*, 2006], and further details can be found there and in *Nordbotten and Celia* [2012]. Section 2.3 contains new results needed to analyze thermal aquifer storage.

### 2.1. Model Equations

We denote the vertical elevation of the compositional and thermal fronts as $\zeta_i(r,t)$, with $i=\{1,2\}$, respectively, where $r$ is the horizontal radial spatial coordinate (cf. again Figure 1). Please note that all notation is summarized in the Notation section at the end of the manuscript. For convention, we denote the elevation of the bottom and top of the aquifer as $\zeta_0$ and $\zeta_3$, and thus $\zeta_0 \le \{\zeta_1,\zeta_2\} \le \zeta_3$. The two fronts separate the three regions, and it follows from the modeling assumptions that there is a constant temperature and composition within each region. As with the fronts, we enumerate the regions from outermost (resident composition and temperature), to the intermediate (injection composition, and resident temperature), to the innermost (injection composition and temperature), and denote the resulting fluid densities and viscosities as $\rho_j$ and $\mu_j$. Similarly, we denote the thicknesses $h_j$ for regions $j=\{1,2,3\}$, with $h_0=\zeta_3-\zeta_0$ defined as the aquifer thickness. The relationships between $\zeta_i$ and $h_j$ are shown in Figure 1, where $h_1$ is the white region, $h_2$ is the light gray region, and $h_3$ is the darker gray region. For clarity we will be consistent with indexing fronts by $i$ and regions by $j$.

In principle, the derivations in these sections are valid for arbitrary density differences, but it is useful to distinguish two cases. We denote as *monotone* when either

$$\rho_1 \ge \rho_2 \ge \rho_3 \quad \text{or} \quad \rho_1 \le \rho_2 \le \rho_3 \tag{2.1}$$

Conversely, we denote as *nonmonotone* when either

$$\rho_1 \le \rho_2 \ge \rho_3 \quad \text{or} \quad \rho_1 \ge \rho_2 \le \rho_3 \tag{2.2}$$

Figure 1 illustrates the first case of equation (2.1). The second case of equation (2.1) is identical, but with the figure flipped vertically, such that the fronts are decreasing (in the form of "\\"). The nonmonotone cases of equation (2.2) combine the monotone cases, so that the two fronts form a "/ \" shape in the former and a "\ /" in the latter. For monotone densities, the first case stated in equations (2.1) leads to

$$h_1=\zeta_1-\zeta_0, \quad h_2=\zeta_2-\zeta_1 \quad \text{and} \quad h_3=\zeta_3-\zeta_2 \tag{2.3}$$

While similarly for nonmonotone densities, the first case stated in equation (2.1) leads to

$$h_1=\zeta_3-\zeta_1, \quad h_2=\zeta_1+\zeta_2-\zeta_0-\zeta_3 \quad \text{and} \quad h_3=\zeta_3-\zeta_2 \tag{2.4}$$

The latter cases stated in equations (2.1) and (2.2) are analogous. The derivation will be valid for all four cases, but when concreteness is needed we consider the monotone cases.

We will use the Dupuit assumption, such that the vertical pressure variation is approximated as fluid-static. Then we can identify a characteristic fluid potential within each of the three regions (at some horizontal datum), and state the integrated (horizontally and angularly) Darcy's laws:

$$U_j = -2\pi r h_j \frac{k}{\mu_j}\frac{\partial p_j}{\partial r} \tag{2.5}$$

Using the assumption that the fluid column is in vertical equilibrium at any spatial point $r$, the fluid potential $p_j$ is independent of the vertical coordinate within each region, and when the regions overlap we obtain the following relationships between the fluid pressures across the two fronts [*Nordbotten and Celia*, 2012]

$$\frac{\partial}{\partial r}\Delta_i p = \Delta_i \rho g \frac{\partial \zeta_i}{\partial r} \tag{2.6}$$

Here we introduce the notation $\Delta_i p = p_{j+1} - p_j$ with $i=j=\{1,2\}$. The integrated mass balance for concentration is then (using that the fluids are considered incompressible):

$$2\pi r\phi \frac{\partial h_1}{\partial t} = -\frac{\partial U_1}{\partial r} \tag{2.7}$$

The coefficient $\phi$ reflects the porosity of the medium. Analogously, the balance equation for thermal energy is stated as

$$2\pi r \frac{\partial h_3}{\partial t} = -\gamma_T \frac{\partial U_3}{\partial r} \tag{2.8}$$

The coefficient $\gamma_T$ reflects the retardation of the thermal front due to the heat capacity of the solid, and is defined as

$$\gamma_T = \frac{\phi\kappa_f}{\phi\kappa_f + (1-\phi)\kappa_s} \tag{2.9}$$

Here $\kappa_f$ and $\kappa_s$ are the thermal heat capacities of the fluid and solid, respectively. Finally, we note that by volume balance, the total flow rate has to equal the injection rate $\Psi$, thus

$$\Psi = U_1 + U_2 + U_3 \tag{2.10}$$

The system of equations (2.5)–(2.8) and (2.10) comprise eight equations for the eight unknowns $U_j$, $p_j$ and $\zeta_i$, and as such is formally a complete model for the evolution.

### 2.2. Dimensionless Form and Self-Similar Scaling

The system of equations stated in section 2.1 can be combined to three equations. We choose $p = p_1$ as the reference pressure for the system, and eliminate the remaining pressures and fluxes to obtain

$$r\phi\frac{\partial h_1}{\partial t} = \frac{\partial}{\partial r}\left[r h_1 \frac{k}{\mu_1}\frac{\partial p}{\partial r}\right] \tag{2.11}$$

$$r\frac{\partial h_3}{\partial t} = \gamma_T \frac{\partial}{\partial r}\left[r h_3 \frac{k}{\mu_3}\frac{\partial}{\partial r}(p - |\Delta_1\rho| g h_1 + |\Delta_2\rho| g h_3)\right] \tag{2.12}$$

$$\left(h_1\mu_1^{-1} + h_2\mu_2^{-1} + h_3\mu_3^{-1}\right)\frac{\partial p}{\partial r} = \frac{-\Psi}{2\pi r k} + h_2\mu_2^{-1}|\Delta_1\rho| g\frac{\partial h_1}{\partial r} + h_3\mu_3^{-1}\left(|\Delta_1\rho| g\frac{\partial h_1}{\partial r} - |\Delta_2\rho| g\frac{\partial h_3}{\partial r}\right) \tag{2.13}$$

Note that the absolute values of density differences occur due to the different ordering of the fluids associated with sign changes in density, as discussed in and after equations (2.3) and (2.4). To obtain a dimensionless form of these equations, we introduce a characteristic density difference in the system, defined as the largest density difference between any two regions (bounded below by the unit constant in order to be able to consider systems with constant density):

$$\Delta\rho = \max\left(|\Delta_1\rho|, |\Delta_2\rho|, |\rho_3 - \rho_1|, \ 1\right) \tag{2.14}$$

Then it is natural to define the dimensionless quantities

$$\Gamma = \frac{\pi\mu_1^{-1}k\Delta\rho g h_0^2}{\Psi}, \quad \lambda_i = \frac{\mu_1}{\mu_{i+1}}, \quad v_i = \frac{|\Delta_i\rho|}{\Delta\rho}, \quad h_j^* = \frac{h_j}{H}, \quad p^* = \frac{p\pi\mu_1^{-1}k}{\Psi}, \quad \tau = \frac{\Psi\phi t}{\pi h_0 k}, \quad \eta = \frac{r}{\sqrt{k}}, \quad \gamma = \phi\gamma_T \tag{2.15}$$

Note that the definition of the gravity number $\Gamma$ differs by a factor 2 from that found in the cited references [*Guo et al*., 2016; *Nordbotten and Celia*, 2006, 2012]. The dimensionless form of equations (2.11)–(2.13) can now be written as (omitting the asterix notation for clarity, and eliminating $h_2$ in favor of $h_1$ and $h_3$):

$$\eta\frac{\partial h_1}{\partial\tau} = \frac{\partial}{\partial\eta}\left[\eta h_1\frac{\partial p}{\partial\eta}\right] \tag{2.16}$$

$$\eta\frac{\partial h_3}{\partial\tau} = \gamma\frac{\partial}{\partial\eta}\left[\eta h_3\lambda_2\frac{\partial}{\partial\eta}(p - \Gamma v_1 h_1 + \Gamma v_2 h_3)\right] \tag{2.17}$$

$$-(\lambda_1 + h_1(1-\lambda_1) + h_3\Delta\lambda)\frac{\partial p}{\partial\eta} = \frac{1}{2\eta} - [(1-h_1)\lambda_1 + h_3\Delta\lambda]\Gamma v_1\frac{\partial h_1}{\partial\eta} + h_3\lambda_2\Gamma v_2\frac{\partial h_3}{\partial\eta} \tag{2.18}$$

These equations admit a self-similar scaling solution by introducing the scaling variable associated with constant injection,

$$\chi = \eta^2/\tau \tag{2.19}$$

This transformation allows the solution of the partial differential equations (2.16)–(2.18) to be expressed in terms of the solution of the set of ordinary differential equations

$$-\chi\frac{dh_1}{d\chi} = 4\frac{d}{d\chi}\left[\chi h_1\frac{dp}{d\chi}\right] \tag{2.20}$$

$$-\chi\frac{dh_3}{d\chi} = 4\gamma\frac{d}{d\chi}\left[\chi h_3\lambda_2\frac{d}{d\chi}(p - \Gamma v_1 h_1 + \Gamma v_2 h_3)\right] \tag{2.21}$$

$$-(\lambda_1 + h_1(1-\lambda_1) + h_3\Delta\lambda)\frac{dp}{d\chi} = \frac{1}{4\chi} - [(1-h_1)\lambda_1 + h_3\Delta\lambda]\Gamma v_1\frac{dh_1}{d\chi} + h_3\lambda_2\Gamma v_2\frac{dh_3}{d\chi} \tag{2.22}$$

Here the notation $\Delta\lambda = (\lambda_2 - \lambda_1)$ is used. These equations are complemented by the mass and energy balance of the system, such that

$$\int_0^\infty (h_2 + h_3)d\chi = 1 \tag{2.23}$$

$$\int_0^\infty h_3 d\chi = \gamma \tag{2.24}$$

Equations (2.20)–(2.22) were first derived by *Nordbotten and Celia*, and briefly analyzed therein [*Nordbotten and Celia*, 2006]. This full system has since then received little attention. By omitting the energy equation (2.21) and setting $h_3 = 0$, a simpler system with a single interface represented by $h_1$ is obtained, which has been extensively studied (see review in *Guo et al*. [2016]).

#### 2.2.1. Remark 2.1

As a mathematical detail, it is important to note that the conservation equations (2.16)–(2.18) and (2.20)–(2.22) should be understood in a weak sense [*LeFloch*, 2002]. In particular, when $\lambda_i \leq 1$ and $\Gamma \to 0$, the solution will be a piston-like displacement, which is represented by discontinuities at $h_1 = 1$ and $h_3 = \gamma$. An appropriate weak formulation can be obtained by formally eliminating equation (2.18) as an algebraic relationship, and multiplying equations (2.16) and (2.17) by test functions before integrating over the positive real line. The test functions must either be chosen from suitable spaces in order to accommodate the constraints (2.23) and (2.24), or these constraints must be enforced through Lagrange multipliers. We will omit this more elaborate analysis herein, and consistently write equations (2.16)–(2.18) and its later derivations as above on their respective strong forms, keeping in mind that we need to allow for the possibility of discontinuities at the locations stated above.

### 2.3. Analytical Results

Equations (2.20)–(2.22) can in general be solved by eliminating (2.22), and solving the resulting two equations using a shooting procedure for the resulting pair of second-order ordinary differential equations in order to satisfy the integral conditions (2.20) and (2.21). While this approach can be made computationally efficient in the case of mass conservation alone, it is not as simple to solve the coupled system, in part due to the degeneracy of the equations at $h_i=\{0,1\}$. For this reason, as well as in the interest of conducting quantitative analysis, we wish to have explicit expressions approximating the solution. A special case of the full system (with $\Delta\lambda=0$ and $\Gamma=0$, which in this context is equivalent to the unrealistic case of no viscosity difference between hot and cold water, and high injection rates) was conducted in *Nordbotten and Celia* [2006]. Herein, we will present the first comprehensive analysis of equations (2.20)–(2.24).

We note that in the context of energy storage, we expect that the changes in fluid densities and viscosities will be small (i.e., $|\lambda_i-1| \ll 1$ and $v_i=\mathcal{O}(1)$), while the injection rate will be appreciable (i.e., $\Gamma \ll 1$). Also, equations (2.7) and (2.8) reveal that the concentration front progresses significantly faster than the thermal front (i.e., $1-\gamma=\mathcal{O}(1)$). To summarize, we will be interested in the limits of

$$0 \leq \{\Gamma, |\epsilon_i|\} \ll 1, v_i=\mathcal{O}(1) \textit{and} 1-\gamma=\mathcal{O}(1) \tag{2.25}$$

where we define $\epsilon_i=\lambda_i-1$, bringing attention to the fact that we make no assumptions on the sign of $\epsilon_i$ or $v_i$ (beyond the sign convention of equations (2.1) and (2.2)). We proceed in two steps: First, we obtain an analytical solution in the $\Gamma \to 0$ limit for the linearized form of equations (2.20)–(2.22), valid for $|\epsilon_i| \ll 1$. Second, we obtain the first-order correction valid for $0 \leq \Gamma \ll 1$ when also $|\epsilon_i| \ll 1$.

#### 2.3.1. Exact Solution for $\Gamma=0$

In the limit of high injection rates, equations (2.20)–(2.22) simplify as follows:

$$\chi \frac{dh_1}{d\chi} = \frac{d}{d\chi}\left[h_1\left(-4\chi\frac{dp}{d\chi}\right)\right] \tag{2.26}$$

$$\chi \frac{dh_3}{d\chi} = \gamma\lambda_2 \frac{d}{d\chi}\left[h_3\left(-4\chi\frac{dp}{d\chi}\right)\right] \tag{2.27}$$

$$\left(-4\chi\frac{dp}{d\chi}\right) = (\lambda_1 - h_1(\lambda_1-1) + h_3\Delta\lambda)^{-1} \tag{2.28}$$

When either $h_1$ or $h_3$ are zero, equations (2.26)–(2.28) are straight-forward to solve for the remaining non-constant function

$$h_1 = \left[\frac{1}{\lambda_1-1}\left(\lambda_1 - \sqrt{\frac{\lambda_1}{\chi}}\right)\right]^{\pm} \quad \text{when} \quad h_3(\chi)=0 \quad \text{and} \quad \lambda_1 > 1 \tag{2.29}$$

$$h_3 = \left[\frac{1}{\Delta\lambda}\left(\sqrt{\frac{\lambda_1\lambda_2\gamma}{\chi}} - \lambda_1\right)\right]^{\pm} \quad \text{when} \quad h_1(\chi)=0 \quad \text{and} \quad \Delta\lambda > 1 \tag{2.30}$$

The notation $f^{\pm}=max\,(0, min\,(1, f))$ herein denotes a function bounded by zero and one. If either $\lambda_1 \leq 1$ or $\Delta\lambda \leq 0$, it follows from the theory of hyperbolic conservation laws, as discussed in Remark 2.1, that the corresponding solutions are Heaviside functions, e.g.,

$$h_1 = H(\chi-1) \quad \text{when} \quad h_3(\chi)=0 \quad \text{and} \quad \lambda_1 \leq 0 \tag{2.31}$$

$$h_3 = 1-H(\chi-\gamma) \quad \text{when} \quad h_3(\chi)=0 \quad \text{and} \quad \Delta\lambda \leq 0 \tag{2.32}$$

By inspection, we see that equations (2.29)–(2.32) hold with $h_1h_3=0$, if

$$\gamma\left(\Delta\lambda^{+}+\lambda_1\right) \leq 1+(\lambda_1-1)^{-} \tag{2.33}$$

The superscript $+$ (respectively, $-$) indicates that only positive (negative) values are considered, e.g., $\Delta\lambda^{+}=\max(0,\Delta\lambda)$. Given assumptions (2.25), we have that $1-\gamma=\mathcal{O}(1)$, and inequality (2.33) will always hold for sufficiently small $|\epsilon_i|$, and thus equations (2.29)–(2.32) form the exact solution of equations (2.26)–(2.28).

### 2.3.2. Approximate Solution for $\Gamma \ll 1$

In general, it does not appear possible to find a closed-form solution for equations (2.20)–(2.24), even for the simpler case where the energy equation (2.21) is omitted [*Guo et al.*, 2016]. As a complement to the exact solution derived in section 2.3.1, we will however also give the lowest-order (with respect to $\Gamma$) linear correction. In this section, we will only consider $\lambda_1 > 1$ and $\Delta\lambda > 0$, since the other cases will be treated better in the following section.

Consider the expansion

$$h_{i,\Gamma}(\chi) = h_{i,0}(\chi) + \Gamma v_i \tilde{h}_i(\chi) = h_{i,0}(\chi) \tag{2.34}$$

We continue to use the a priori assumption that $h_1 h_3 = 0$, and insert equation (2.34), for $i=1$, into equations (2.20)–(2.22), and expanding the fraction by the lowest-order Taylor series:

$$\begin{aligned}\frac{\chi}{4}\left(\frac{dh_{1,0}}{d\chi} + \Gamma v_1 \frac{d\tilde{h}_1}{d\chi}\right) = \frac{d}{d\chi}\Bigg[\sqrt{\frac{\chi}{\lambda_1}}\left(1 + (\lambda_1 - 1)\Gamma v_1 \sqrt{\frac{\chi}{\lambda_1}}\tilde{h}_1\right)\left(h_{1,0} + \Gamma v_1 \tilde{h}_1\right) \\ \left(\frac{1}{4} - \chi\left(1 - h_{1,0} - \Gamma v_1 \tilde{h}_1\right)\lambda_1 \Gamma v_1 \left(\frac{dh_{1,0}}{d\chi} + \Gamma v_1 \frac{d\tilde{h}_1}{d\chi}\right)\right)\Bigg]\end{aligned} \tag{2.35}$$

The terms solving equation (2.26) equate to zero, and by retaining low-order terms we obtain after a few manipulations

$$\chi \frac{d\tilde{h}_1}{d\chi} = \frac{d}{d\chi}\left[\chi \tilde{h}_1 + 2\left(\frac{\lambda_1^2(\chi^{-1}+1)}{(\lambda_1 - 1)^3} - \sqrt{\frac{\lambda_1}{\chi}}\frac{\lambda_1(\lambda_1+1)}{(\lambda_1-1)^3}\right)\right] \tag{2.36}$$

where the solution is

$$\tilde{h}_1 = \frac{2}{(\lambda_1 - 1)^3}\left(\frac{\lambda_1}{\chi}\right)^2 - \frac{(\lambda_1 + 1)}{(\lambda_1 - 1)^3}\left(\frac{\lambda_1}{\chi}\right)^{3/2} \tag{2.37}$$

Combining equation (2.37) with equation (2.20), we obtain

$$h_{1,\Gamma} = \left[\frac{1}{\lambda_1 - 1}\left(\lambda_1 - \left(\frac{\lambda_1}{\chi}\right)^{\frac{1}{2}} - \Gamma v_1 \frac{\lambda_1 + 1}{(\lambda_1 - 1)^2}\left(\frac{\lambda_1}{\chi}\right)^{\frac{3}{2}} + \frac{2\Gamma v_1}{(\lambda_1 - 1)^2}\left(\frac{\lambda_1}{\chi}\right)^2\right)\right]^{\pm} \tag{2.38}$$

Note that this solution is only valid when $\frac{dh_{1,\Gamma}}{d\chi} \geq 0$, thus when in the range where the solution is applicable

$$\chi^{\frac{3}{2}} + 3\Gamma v_1 \frac{(\lambda_1 + 1)\lambda_1}{(\lambda_1 - 1)^2}\chi^{\frac{1}{2}} - \frac{8\Gamma v_1 \lambda_1^{3/2}}{(\lambda_1 - 1)^2} \geq 0 \tag{2.39}$$

Similarly, we obtain by the same procedure

$$h_{3,\Gamma} = \left[\frac{1}{\Delta\lambda}\left(-\lambda_1 + \left(\frac{\lambda_1\lambda_2\gamma}{\chi}\right)^{\frac{1}{2}} + \Gamma v_2 \frac{\lambda_1 + \lambda_2}{\Delta\lambda^2}\left(\frac{\lambda_1\lambda_2\gamma}{\chi}\right)^{\frac{3}{2}} - \frac{2\Gamma v_2}{\Delta\lambda^2}\left(\frac{\lambda_1\lambda_2\gamma}{\chi}\right)^2\right)\right]^{\pm} \tag{2.40}$$

With a similar constraint to equation (2.39),

$$\chi^{\frac{3}{2}} + 3\Gamma v_2 \frac{(\lambda_1 + \lambda_2)\lambda_1\lambda_2\gamma}{\Delta\lambda^2}\chi^{\frac{1}{2}} - \frac{8\Gamma v_2(\lambda_1\lambda_2\gamma)^{3/2}}{\Delta\lambda^2} \geq 0 \tag{2.41}$$

Note that the mass and energy balance equations (2.23)–(2.24) are not satisfied exactly by the approximations in this section.

### 2.3.3. Approximate Solution for $\Gamma \ll 1$ and $|\epsilon_i| \ll 1$

The inequalities (2.39) and (2.41) are quite restrictive, in particular in the case of $\epsilon_1 \ll 1$ and $\Delta\epsilon = \Delta\lambda \ll 1$. However, it is possible to obtain an approximation to the solution for $0 < \{\Gamma, |\epsilon_i|\} \ll 1$ directly, which also satisfies the balance conditions (2.23) and (2.24). In this section, we will make numerous a priori assumptions regarding the solution in our derivation, noted by an underscore, these will be validated *post hoc* at the end of the section. In particular, we make the a priori assumption that the solution depends continuously on $\Gamma$ and $\epsilon_i$.

We proceed by linearizing the pressure equation (2.22). Exploiting that $|\epsilon_i| \ll 1$ we then obtain

$$-\frac{dp}{d\chi} = \left[\frac{1}{4\chi} - [(1-h_1)(1+\epsilon_1)+h_3\Delta\epsilon]\Gamma v_1 \frac{dh_1}{d\chi} + h_3(1+\epsilon_2)\Gamma v_2 \frac{dh_3}{d\chi}\right](1-\epsilon_1+h_1\epsilon_1-h_3\Delta\epsilon) \tag{2.42}$$

Further eliminating the pressure by inserting equation (2.42) into (2.20) and (2.21) leads to:

$$\chi\frac{dh_1}{d\chi} = 4\frac{d}{d\chi}\left[h_1(1-\epsilon_1+h_1\epsilon_1-h_3\Delta\epsilon)\left(\frac{1}{4} - [(1-h_1)(1+\epsilon_1)+h_3\Delta\epsilon]\Gamma v_1\chi\frac{dh_1}{d\chi} + h_3(1+\epsilon_2)\Gamma v_2\chi\frac{dh_3}{d\chi}\right)\right] \tag{2.43}$$

and

$$\begin{aligned}\chi\frac{dh_3}{d\chi} = 4\gamma\frac{d}{d\chi}\Bigg[&h_3\lambda_2(1-\epsilon_1+h_1\epsilon_1-h_3\Delta\epsilon)\left(\frac{1}{4} - [(1-h_1)(1+\epsilon_1)+h_3\Delta\epsilon]\Gamma v_1\chi\frac{dh_1}{d\chi} - h_3(1+\epsilon_2)\Gamma v_2\chi\frac{dh_3}{d\chi}\right)\\ &+\chi h_3\lambda_2\frac{d}{d\chi}(\Gamma v_1 h_1 - \Gamma v_2 h_3)\Bigg]\end{aligned} \tag{2.44}$$

To obtain an approximate solution to equations (2.43) and (2.44), we are motivated by the previous section to use assumptions (2.25) together with inequality (2.33) as the basis for the ansatz that for any $\chi$, either $h_1=0$ or $h_3=0$, or both. Then equations (2.43) and (2.44) decouple, and simplify to

$$\chi\frac{dh_1}{d\chi} = 4\frac{d}{d\chi}\left[h_1(1-\epsilon_1+h_1\epsilon_1)\left(\frac{1}{4} - [(1-h_1)(1+\epsilon_1)]\Gamma v_1\chi\frac{dh_1}{d\chi}\right)\right] \tag{2.45}$$

$$\chi\frac{dh_3}{d\chi} = 4\gamma\frac{d}{d\chi}\left[h_3(1+\epsilon_2)(1-\epsilon_1-h_3\Delta\epsilon)\left(\frac{1}{4} + h_3(1+\epsilon_2)\Gamma v_2\chi\frac{dh_3}{d\chi}\right) - (1+\epsilon_2)\Gamma v_2\chi h_3\frac{dh_3}{d\chi}\right] \tag{2.46}$$

Consider first equation (2.45), and expand the derivatives on the right hand side to obtain

$$\begin{aligned}\frac{\chi}{4}h_1' = &\frac{1-\epsilon_1+2h_1\epsilon_1}{4}h_1' - h_1(1-\epsilon_1+h_1\epsilon_1)[(1-h_1)(1+\epsilon_1)]\Gamma v_1\left(h_1'+\chi_{1,0}h_1'\prime\right)\\ &-\left(1-2h_1-\epsilon_1+4h_1\epsilon_1-3h_1^2\epsilon_1\right)(1+\epsilon_1)\Gamma v_1\chi_{1,0}\left(h_1'\right)^2\end{aligned} \tag{2.47}$$

We reduce the spatial heterogeneity of equation (2.47) by considering in principle a fixed-point iteration, where on the right hand side we use the previous iteration where indicated by $\chi_{1,0}$. For the first iteration, $\chi_{1,0}$ is chosen as equation (2.31). We make the ansatz that equation (2.47) can be well approximated by the linear solution:

$$h_{1,\Gamma}(\chi) = \left[\frac{\chi-(1-a_1)}{2a_1}\right]^{\pm} \quad \text{for} \quad h_{3,\Gamma}(\chi)=0 \tag{2.48}$$

The subscript $\Gamma$ indicates that the solution is valid for $\Gamma > 0$. Note that the solution form given in equation (2.48) automatically satisfies mass conservation, equation (2.23). From equation (2.48) we then obtain (by retaining only low-order terms, and subsequently noting that since $a_1=0$ for $\Gamma=\epsilon_1=0$, then by the assumption that the solution depends continuously on the parameters, the solution is close to discontinuous, and therefore $\left(h_1'\right)^2 \gg h_1'$):

$$\frac{1}{4}\left(\chi-1+\epsilon_1-2\epsilon_1\frac{\chi-(1-a_1)}{2a_1}\right) = -\left(1-2\frac{\chi-(1-a_1)}{2a_1}\right)\Gamma v_1\left(\frac{1}{2a_1}\right) \tag{2.49}$$

Some straight-forward manipulations and then collecting terms proportional to $\chi$ lead to the following solution for $a_1$

$$a_1 = \frac{\epsilon_1 + \left(\epsilon_1^2+8\Gamma|v_1|\right)^{1/2}}{2} \tag{2.50}$$

Equations (2.48) and (2.50) together represent an approximate solution for $h_1$ valid for small $\epsilon$ and $\Gamma$, as desired. In order to make some comments relating to previous work, we note the following special cases:

$$\text{For} \quad \Gamma=0 \quad \text{then} \quad a_1=\epsilon_1^+ \tag{2.51}$$

$$\text{For} \quad \epsilon_1=0 \quad \text{then} \quad a_1=(2\Gamma v_1)^{\frac{1}{2}} \tag{2.52}$$

$$\text{For} \quad \epsilon_1^2 \ll 8\Gamma|v_1| \quad \text{then} \quad a_1 = (2\Gamma v_1)^{\frac{1}{2}}\left(1+\frac{\epsilon_1^2}{16\Gamma v_1}\right)+\frac{\epsilon_1}{2} \tag{2.53}$$

$$\text{For} \quad \epsilon_1^2 \gg 8\Gamma|v_1| \quad \text{then} \quad a_1 = \epsilon_1^+ + 2\frac{\Gamma v_1}{|\epsilon_1|} \tag{2.54}$$

The sign of $\epsilon_1$ enters into equations (2.53) and (2.54), reflecting the change from stable to unstable displacement. In the setting of a single front (no energy equation), equations (2.52) and (2.54) (but only the branch where $\epsilon_1 \leq 0$) were derived by Guo et al. using a slightly different approach [*Guo et al*., 2016]. The present analysis thus unifies their separate treatment of these cases and substantially generalizes their results, in particular for $\epsilon_1 > 0$. This generalization is critical for the applicability to energy storage.

Equation (2.46) is treated in analogous fashion to equation (2.45). Thus we use an ansatz of

$$h_{3,\Gamma}(\chi) = \left[\frac{-\chi+\gamma(1+a_2)}{2\gamma a_2}\right]^{\pm} \quad \text{for} \quad h_{1,\Gamma}(\chi)=0 \tag{2.55}$$

where we determine by a similar calculation as above the expression for $a_2$

$$a_2 = \frac{\Delta\epsilon+\left((\Delta\epsilon)^2+8\Gamma v_2\right)^{1/2}}{2} \tag{2.56}$$

Special cases analogous to equations (2.51)–(2.54) can be obtained in the same manner. Equations (2.48), (2.50), and (2.55–2.56) provide the full set of approximations to the linearized equations.

#### 2.3.4. Remark 2.2

We now verify the initial a priori structural assumptions made in the derivation. This does not constitute a proof that the assumptions are correct – it is rather a verification that the final approximation does not contradict any of the assumptions made in the derivation. First, from equations (2.50) and (2.56) we see that $a_1 = \mathcal{O}\left(\Gamma^{\frac{1}{2}}+\epsilon_1\right)$ and $a_2 = \mathcal{O}\left(\Gamma^{\frac{1}{2}}+\Delta\epsilon\right)$, thus the solution depends continuously (in the Hölder sense) on the parameters $\Gamma$ and $\epsilon_i$. Second, we derive from equations (2.48), (2.50), (2.55), and (2.56), that $h_1 h_3 = 0$ whenever

$$(1+a_2)\gamma \leq 1-a_1 \tag{2.57}$$

Since we already established that $a_1 \ll 1$, this holds by the same argument as inequality (2.33). Finally, the ansatz that the solution is well approximated by a linear solution is verified by noting that (2.50) also resolves the constant terms in equation (2.49), and similarly for (2.56).

### 2.4. Qualitative Summary of Analytical Results

Sections 2.3.1–2.3.3 provide several approximations to the self-similar ordinary differential equations presented in equations (2.16)–(2.18). We summarize their main qualitative properties in Table 1.

From a practical perspective, the exact analytical solution from section 2.3.1 may be applied to moderate values of $\Gamma < 0.1$ [*Nordbotten and Celia*, 2006]. However, it will frequently be of interest to have an understanding of the impact of density differences and the injection rate, in which case the solutions of sections 2.3.2 and 2.3.3 are needed. The perturbation expansion from section 2.3.2 is a higher-order approximation, and shares the common features of such approximations that it has high accuracy when valid, however the range of validity is (severely) limited. In contrast, the solution based on linearization in section 2.3.3 is a low-order approximation, and consequently significantly more robust, at the cost of accuracy.

**Table 1.** Qualitative Summary of the Various Results Presented in Sections 2.3.1, 2.3.2, and 2.3.3

| Section | Type | Validity | Applicability |
|---|---|---|---|
| 2.3.1 | Analytical | $\Gamma=0$<br>$\epsilon \leq \mathcal{O}(1)$ | Very high injection rates |
| 2.3.2 | Perturbation | $\Gamma \leq \mathcal{O}(\epsilon^2)$<br>$\epsilon \leq \mathcal{O}(1)$ | High injection rates |
| 2.3.3 | Linearization | $\{\Gamma, \epsilon\} \ll 1$ | Moderate injection rates, moderate viscosity ratios |

## 3. Validation

In this section, we wish to validate the approximate solutions derived in section 2.3. As benchmark, we will use a standard finite-volume approximation (with explicit treatment of first-order terms and implicit treatment of second-order terms) of the dimensionless governing equations as

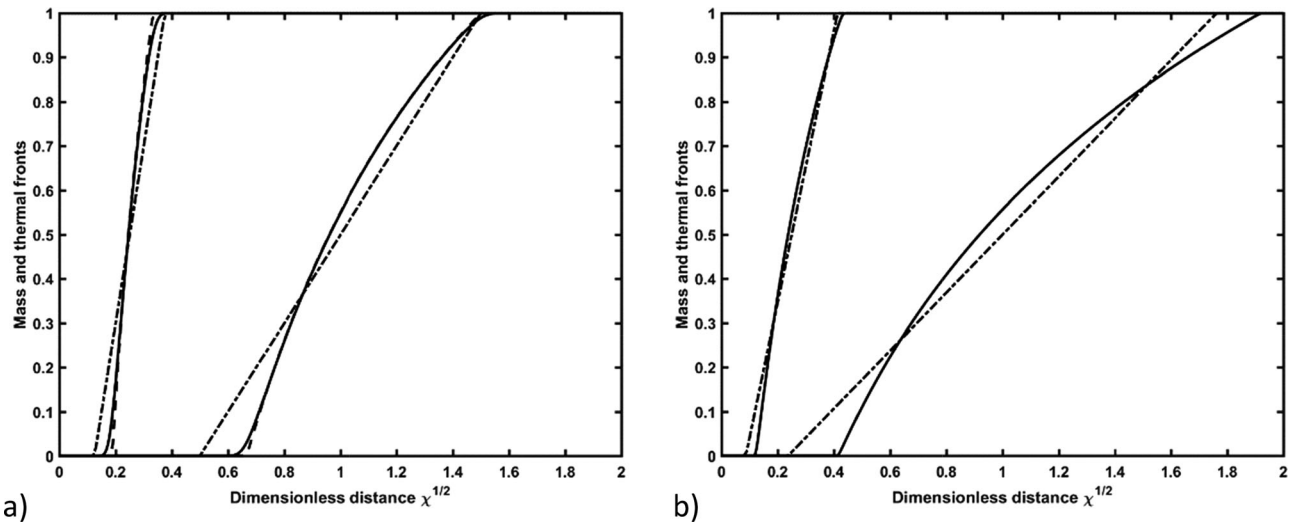


**Figure 2.** Example solutions with (left) $\Gamma=0$ and (right) $\Gamma=0.1$. In both figures $\epsilon_1=\Delta\epsilon=0.5$. Solid lines indicate numerical solution, dashed lines analytical solution from section 2.3.1 (only in left figure) and dash-dotted lines indicate the approximate linear solutions from section 2.3.3. The solutions from section 2.3.2 coincide with the solid line in the left figure, and are not applicable in the right figure.

stated in equations (2.16)–(2.18) [*LeVeque*, 1992]. Throughout these validations, we will conform with the relevant conditions for energy storage outlined in assumptions (2.25), and thus only consider parameter ranges of $-0.5 < \{\epsilon_1, \Delta\epsilon\} \leq 1$, $0 \leq \Gamma \leq 0.25$ and $\gamma=0.1$. The parameters $v_i$ are taken as unity. We note that the ranges chosen for $\epsilon_i$ and $\Gamma$ are purposefully chosen as larger than what is typically associated with $\ll 1$, in order to explore the range of validity of the approximations derived above.

We will conduct the validation in two steps. First, since the solutions provided in section 2.3.1 represent the exact asymptotic solutions to the system when $\Gamma \to 0$, we use these solutions to validate our numerical implementation of equations (2.16)–(2.18) as well as the suitability of the linearized equations derived in section 2.3.2 and 2.3.3 when $\Gamma \to 0$. Second, we validate the approximate solutions to the linearized equations obtained in sections 2.3.2 and 2.3.3 for $\Gamma > 0$.

As means of illustration, in Figure 2 we show typical solution profiles, in both cases at the extreme range of investigated unfavorable viscosity ratios, $\epsilon_1=0.5$ and $\Delta\epsilon=0.5$. For these figures, we use $\gamma=0.25$ to make the thermal front more visible in the figure. In Figure 2 (left), we first consider the case of high injection rates with $\Gamma=0$. We show the numerical solution (solid lines, denoted $h_{i,N}$ in the following), the analytical solution given in equations (2.29) and (2.30) (dashed lines, denoted $h_{i,A}$ in the following) and the (in this case exact) solution to the linearized model given in equations (2.48) and (2.55) (dash-dotted lines, denoted $h_{i,L}$ in the following). In Figure 2 (right), we consider the same case with finite injection rate, $\Gamma=0.1$, with the same viscosity ratios. Here, there is no analytical solution, and we thus only show the numerical solution and the now approximate solution of the linearized model. Note that these parameters violate inequality (2.57), which can be seen from the figure as there is a region where both $h_1$ and $h_3$ are nonzero. We do not show the perturbation solution from section 2.3.2, as it is not valid for these parameters.

Whenever we refer to an approximation error, we imply the $L_1$ error measured in the $\chi$ coordinate, e.g., for two solutions $h_{i,a}$ and $h_{i,b}$, the approximation error of one to the other is denoted

$$e_{i,a,b}=\frac{\int_0^\infty |h_{i,a}(\chi)-h_{i,b}(\chi)|d\chi}{\{1,\ \gamma\}_i} \tag{3.1}$$

The normalization of the errors by 1 and $\gamma$, respectively, is chosen due to the characteristic scale of the solutions given by equations (2.23) and (2.24). For reference, the errors in Figure 2 (left) are $e_{i,A,N}=[2.7,\ 10.1]\cdot 10^{-3}$ and $e_{i,A,L}=[59,\ 68]\cdot 10^{-3}$, while the differences in Figure 2 (right) are $e_{i,N,L}=[6.6,\ 3.0]\cdot 10^{-2}$. The numerical grid used for these calculations had 2500 grid points, and this grid is also used for all examples in the validation study which follows. While in this example the linearization error dominates the numerical

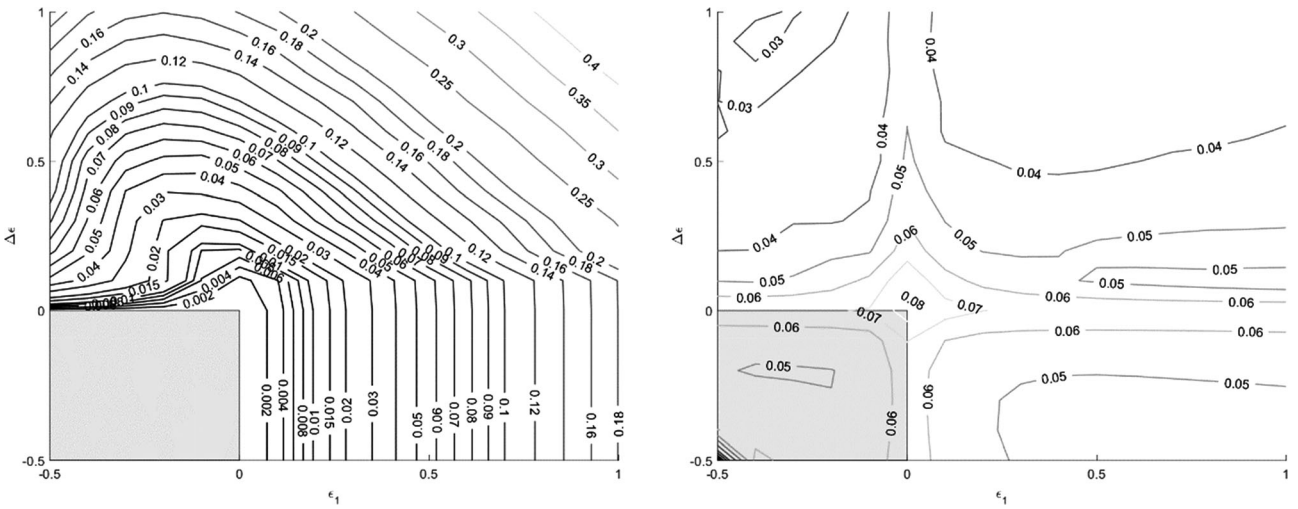

**Figure 3.** Error in the (left) linearized solution and (right) numerical approximation for the case where an exact analytical solution is known ($\Gamma=0$). The light gray area indicates the region in parameter space where the solution is discontinuous (and where the linearized solution is exact).

error, we note that for sufficiently small $\epsilon_i$ and $\Gamma$, the converse will inevitably be true, and the numerical approximation will be larger than the linearization error.

All computations were performed using the Matlab environment. Figures 3 and 4 below comprise 1536 data points, each representing a full simulation of equations (2.16)–(2.18), in addition to the evaluation of the relevant analytical and approximate solutions. The full set of simulations takes around 24 h on a standard desktop computer.

### 3.1. Validation of Numerical Implementation and Linearized Equations for $\Gamma=0$

Within this subsection, we consider only $\Gamma=0$. As a benchmark for our comparisons, we use the fact that equations (2.29)–(2.32) represent the exact solutions to equations (2.16)–(2.18) in this limit. This allows us to verify the accuracy of our numerical approximation, which we will use as benchmark in the subsequent section. Separately, we can assess the error associated with the linearization in section 2.3.3 by comparing the solutions given in that section to those of equations section 2.3.1.

In Figure 3, we plot the errors $\sum_i e_{i,A,N}$ and $\sum_i e_{i,A,L}$ for the full range of parameters considered. The light gray area of the plot indicates the parameter regimes where the solution is discontinuous for both

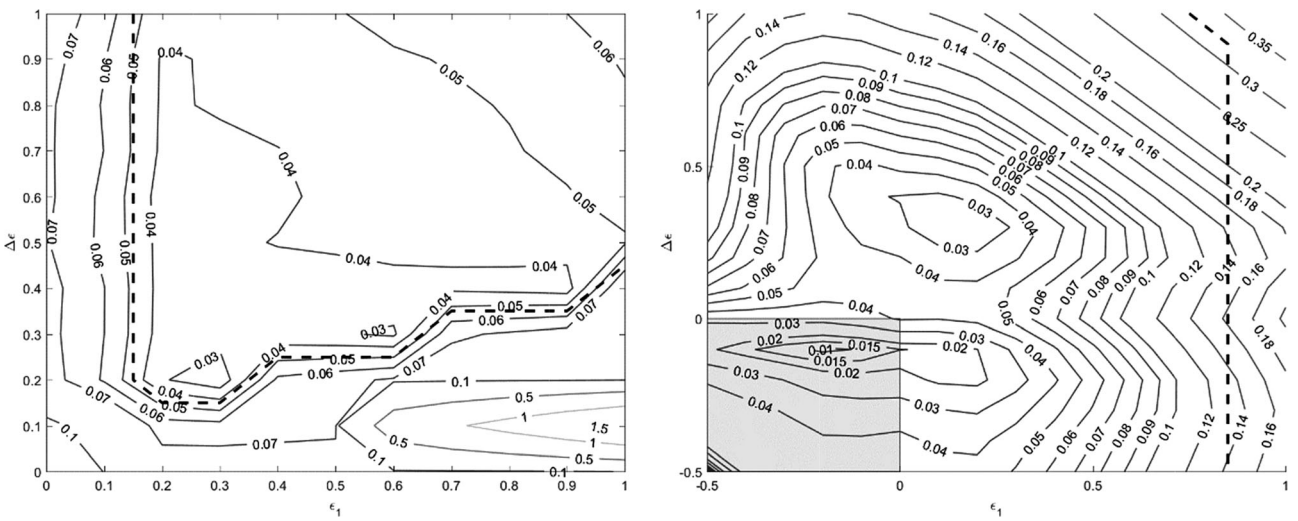

**Figure 4.** Difference between numerical approximation and (left) perturbation and (right) linearized solution for $\Gamma=2.5\cdot10^{-3}$. The dashed lines indicate the regions of validity for the perturbation solution (above the line in the left figure) and the linearized solution (below the line in the right figure), respectively. The range plotted in the left figure does not include negative values as the perturbation solution is not valid in this region.

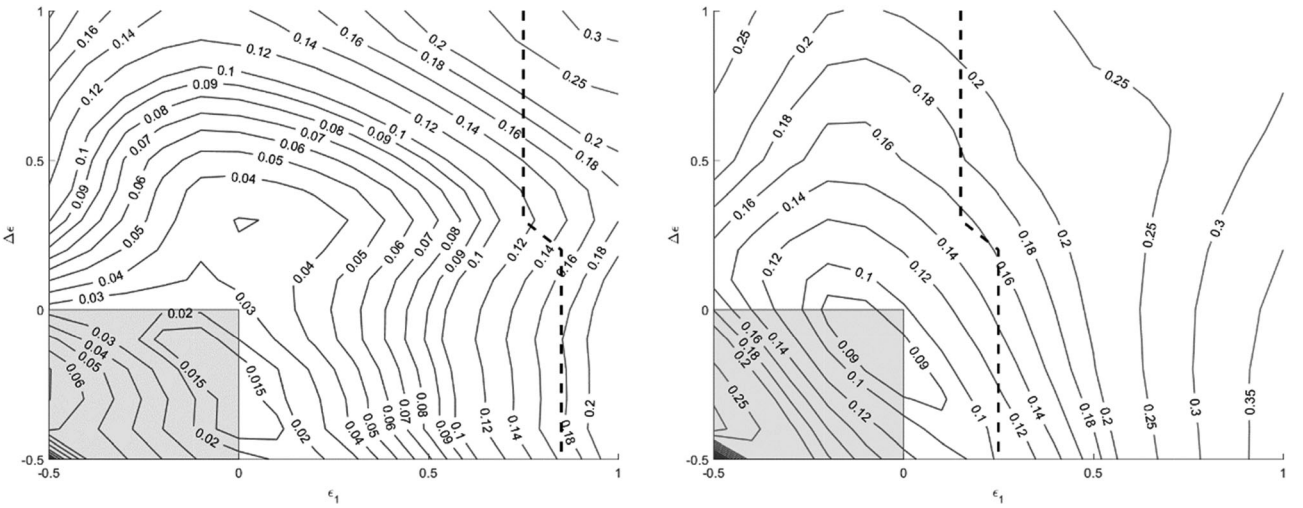

**Figure 5.** Difference between numerical approximation and linearized solution for increasing $\Gamma=\{0.025,\ 0.25\}$, left and right. In each figure, the region where the linearized solution is valid is to the left of the dashed line.

interfaces, e.g., where both $\epsilon_1 \leq 0$ and $\Delta\epsilon \leq 0$. In this region the linearized solution is exact, and $\sum_i e_{i,A,L}=0$. Figures 3 (and later Figure 4) is computed with a spacing of 0.05, thus each figure consists of 256 data points.

We find that the numerical error is in general less than $\sum_i e_{i,A,N} < 0.05$ where the solution is smooth. However, there is a clear peak in the numerical error (due to numerical dispersion) at the limiting case of discontinuous solutions, $\epsilon_1=\Delta\epsilon=0$. The numerical scheme is formally first-order consistent, and first-order convergence was in general observed with respect to grid spacing (results not shown). Similarly, the linearization error is bounded within this parameter regime by the heuristic expression $\sum_i e_{i,A,N} < 0.2\left(\epsilon_1^+ + \Delta\epsilon^+\right)$.

### 3.2. Validation of Linearized and Perturbation Solutions for $\Gamma>0$

Within this subsection, we wish to validate the approximate solutions obtained for $\{\Gamma, |\epsilon_i|\} \ll 1$ in section 2.3.2, as stated in equations (2.48), (2.50), (2.55), and (2.56). Since we do not have an analytical solution to use as reference, we will take the numerical approximation of equations (2.16)–(2.18) as reference solutions. From the previous section, we anticipate that the reference solution is accurate to approximately $5 \cdot 10^{-2}$, which will prove to be sufficient.

We consider first a low value of $\Gamma=2.5 \cdot 10^{-3}$. For these high injection rates, both the perturbation solution as well as the linearized solutions are applicable. Figure 4 illustrate the differences between the numerical reference solution and these approximate solutions. In the figures, we have indicated by a dashed line the region of validity for the respective approximations. Thus the perturbation solution is valid above the dashed line in Figure 4 (left), while the linearization solution is valid to the left of the dashed line in Figure 4 (right). Also emphasized in Figure 4 (right) is the region where both $\epsilon_1 \leq 0$ and $\Delta\epsilon \leq 0$. In this region the viscous forces act to stabilize the front while the gravitational forces tend to destabilize.

For higher values of $\Gamma$, the perturbation solution is no longer applicable. Thus, in Figures 5 we show the difference only between the numerical and linear approximations $\sum_i e_{i,N,L}$ for two larger values of $\Gamma=\{0.025,\ 0.25\}$.

From Figures 3–5 we note that the linear approximation is satisfactory throughout the investigated parameter range, with $\sum_i e_{i,N,L} < 0.4$ for all values, and $\sum_i e_{i,N,L} < 0.3$ for values of $\Gamma$ and $\epsilon_i$ satisfying inequality (2.57). Figure 4 reveals that the perturbation solution is highly accurate when applicable, but the range of applicability is limited.

### 3.3. Characteristic Values of Dimensionless Groups

It is a fundamental assumption herein that the relevant dimensionless groups $\Gamma v_i$ and $\epsilon_i$ are relatively small. We will quantify this by considering data from field injection sites in Alberta, Canada.

**Table 2.** Data and Dimensionless Parameters From 24 Acid Gas Injection Sites in Alberta, Canada[a]

| Site | P (MPa) | T (C) | $\phi$ (%) | $h_0$ (m) | $k$ (mD) | $\Psi$ ($m^3$/s) | $\rho_1$ (kg/$m^3$) | $\mu_1$ (mPa.s) | $\rho_2$ (kg/$m^3$) | $\mu_2$ (mPa.s) | $\rho_3$ (kg/$m^3$) | $\mu_1$ (mPa.s) | $\gamma$ | $\epsilon_1$ | $\Delta\epsilon$ | $\Gamma v_1$ | $\Gamma v_2$ – |
|---|---|---|---|---|---|---|---|---|---|---|---|---|---|---|---|---|---|
| 1 | 13.3 | 58 | 6 | 15 | 30 | 2.30 | 1084 | 0.60 | 1015 | 0.52 | 991 | 0.32 | 0.02 | 0.15 | 0.75 | 1.0E-2 | 1.4E-2 |
| 2 | 16.7 | 57 | 18 | 10 | 186 | 0.31 | 1117 | 0.66 | 1017 | 0.53 | 994 | 0.32 | 0.10 | 0.24 | 0.83 | 2.7E-1 | 3.4E-1 |
| 3 | 11.2 | 56 | 5 | 18 | 40 | 0.67 | 1175 | 0.78 | 1016 | 0.54 | 992 | 0.32 | 0.01 | 0.44 | 0.97 | 1.2E-1 | 1.4E-1 |
| 4 | 9.5 | 53 | 10 | 8 | 100 | 1.15 | 1086 | 0.65 | 1016 | 0.57 | 993 | 0.33 | 0.04 | 0.15 | 0.80 | 1.8E-2 | 2.5E-2 |
| 5 | 15.7 | 71 | 7 | 10 | 16 | 0.70 | 1175 | 0.64 | 1009 | 0.44 | 983 | 0.28 | 0.02 | 0.47 | 0.84 | 1.8E-2 | 2.1E-2 |
| 6 | 16.7 | 76 | 12 | 13 | 30 | 1.18 | 1112 | 0.50 | 1007 | 0.41 | 980 | 0.26 | 0.05 | 0.23 | 0.67 | 2.8E-2 | 3.5E-2 |
| 7 | 8.9 | 45 | 13 | 4 | 6 | 0.45 | 1089 | 0.74 | 1020 | 0.65 | 998 | 0.37 | 0.06 | 0.14 | 0.88 | 6.2E-4 | 8.1E-4 |
| 8 | 11.3 | 52 | 4 | 81 | 9 | 0.26 | 1093 | 0.67 | 1018 | 0.58 | 995 | 0.34 | 0.01 | 0.16 | 0.82 | 7.9E-1 | 1.0E+0 |
| 9 | 13.7 | 60 | 20 | 29 | 6 | 0.27 | 1114 | 0.63 | 1015 | 0.51 | 990 | 0.31 | 0.11 | 0.24 | 0.80 | 9.1E-2 | 1.1E-1 |
| 10 | 15.7 | 64 | 12 | 9 | 9 | 1.11 | 1007 | 0.46 | 1013 | 0.48 | 988 | 0.30 | 0.05 | -.04 | 0.59 | 2.8E-4 | 8.2E-4 |
| 11 | 24.7 | 103 | 9 | 60 | 137 | 0.21 | 1065 | 0.36 | 993 | 0.30 | 963 | 0.21 | 0.03 | 0.20 | 0.51 | 1.5E+1 | 2.1E+1 |
| 12 | 27.0 | 100 | 6 | 10 | 75 | 0.37 | 1090 | 0.39 | 996 | 0.31 | 966 | 0.22 | 0.02 | 0.27 | 0.56 | 1.5E-1 | 2.0E-1 |
| 13 | 20.2 | 70 | 8 | 10 | 115 | 0.31 | 1055 | 0.48 | 1012 | 0.44 | 986 | 0.28 | 0.03 | 0.10 | 0.63 | 1.0E-1 | 1.6E-1 |
| 14 | 20.0 | 76 | 12 | 10 | 9 | 0.57 | 1048 | 0.44 | 1008 | 0.41 | 982 | 0.26 | 0.05 | 0.08 | 0.59 | 4.4E-3 | 7.3E-3 |
| 15 | 13.8 | 38 | 6 | 10 | 14 | 0.45 | 1273 | 1.32 | 1025 | 0.73 | 1004 | 0.40 | 0.02 | 0.80 | 1.52 | 1.8E-2 | 1.9E-2 |
| 16 | 7.5 | 35 | 22 | 40 | 67 | 0.98 | 1061 | 0.82 | 1023 | 0.78 | 1004 | 0.41 | 0.13 | 0.05 | 0.93 | 1.5E-1 | 2.3E-1 |
| 17 | 7.7 | 53 | 10 | 4 | 346 | 0.61 | 1052 | 0.60 | 1016 | 0.57 | 992 | 0.33 | 0.04 | 0.06 | 0.74 | 1.7E-2 | 2.8E-2 |
| 18 | 16.5 | 63 | 11 | 24 | 10 | 0.28 | 1118 | 0.61 | 1014 | 0.49 | 989 | 0.30 | 0.04 | 0.25 | 0.78 | 1.1E-1 | 1.3E-1 |
| 19 | 13.1 | 61 | 12 | 13 | 13 | 2.20 | 1130 | 0.65 | 1014 | 0.50 | 989 | 0.31 | 0.05 | 0.30 | 0.83 | 5.5E-3 | 6.7E-3 |
| 20 | 13.1 | 61 | 12 | 13 | 32 | 3.19 | 1078 | 0.57 | 1014 | 0.50 | 989 | 0.31 | 0.05 | 0.14 | 0.73 | 5.8E-3 | 8.1E-3 |
| 21 | 15.5 | 70 | 5 | 40 | 27 | 0.53 | 1161 | 0.63 | 1010 | 0.44 | 984 | 0.28 | 0.01 | 0.43 | 0.83 | 6.0E-1 | 7.1E-1 |
| 22 | 15.5 | 65 | 6 | 5 | 109 | 0.55 | 1084 | 0.55 | 1013 | 0.47 | 987 | 0.29 | 0.02 | 0.16 | 0.71 | 2.0E-2 | 2.7E-2 |
| 23 | 23.1 | 82 | 12 | 26 | 1 | 1.90 | 1107 | 0.48 | 1006 | 0.38 | 979 | 0.25 | 0.05 | 0.27 | 0.65 | 2.3E-3 | 2.9E-3 |
| 24 | 14.8 | 77 | 10 | 10 | 130 | 3.39 | 1113 | 0.52 | 1005 | 0.40 | 978 | 0.26 | 0.04 | 0.28 | 0.69 | 2.5E-2 | 3.1E-2 |

[a]Site numbers correspond to the references [*Bachu and Carroll*, 2005; *Bachu et al*., 2005]. "P" and "T" are pressure and temperature, respectively, all other symbols correspond to notation in section 2. In lieu of data, the heat capacities of rock and water were taken as 0.8 and 4.2 kJ/C, respectively. All units are standard abbreviations of (factors of) SI units, with the exception of permeability, which is in milli-Darcy (mD). We have shaded gray the sites that violate inequality (2.57), as well as parameters $\epsilon_1$, $\Delta\epsilon$ and $\Gamma v_i$ which are outside the range investigated in section 3.2.

We will base our analysis on the acid gas injection storage sites analyzed by Bachu and coworkers [*Bachu et al*., 2005; *Bachu and Carroll*, 2005]. In particular, we will consider these storage operations as analogues with respect to the variability in injection rates and geological conditions which may be encountered with wide-spread thermal energy storage. As such, we will take their reported geological data, as well as the volumetric injection rates (at *in situ* conditions). The only alteration we consider is to replace the injected gas by heated water. For simplicity, we will herein consider only the injection of sea water at 3.5% salinity, and we will calculate the relevant densities and viscosities based on the initial pressures of the storage units, as well as the initial temperature [*Nayar et al*., 2016]. We will in all cases consider the injected water to be always 40°C warmer than the storage formation.

The relevant data, extracted from the references with the adjustments given above, are summarized in Table 2. For all sites, $\gamma \leq 0.15$, confirming that this number can be considered small. With respect to viscosity, we find that for all but one of the cases considered, the viscosities satisfy $\epsilon_i < 0.5$ and $\Delta\epsilon < 1$. For those sites where injection rates are high ($\Gamma$=0), the validation of the perturbation solution in section 3.2 suggests that the analytical solution given in sections 2.3.1 and 2.3.2 are applicable.

In terms of the actual injection rates from the sites considered, we see that all but one sites have values of $\Gamma v_i \leq 1$, while for 20 of 24 sites we have values of $\Gamma v_i \leq 0.25$. Similarly, while all sites have $\Delta\epsilon > 0.5$, only a single site has $\Delta\epsilon > 1$. Thus the significant majority of sites fall within the range of values considered for the linearized solution in section 3.2. When we consider the applicability of the linearized solution given in section 2.3.3, we find that equation (2.57) is satisfied in all but the four cases where $\Gamma v_i > 0.25$. The sites which fail equation (2.57) are all characterized by low injection rates, relative to the permeability and thickness of the formation.

It is also interesting to note injection site number 10, where a nonmonotone density situation (in the sense of equation (2.2)) arises, since the ambient fluid density, $\rho_1$, is smaller than the density of the injected fluid at the same temperature conditions.

Based on this moderate sample of analogue sites, we thus conclude that the expressions derived herein are applicable to the majority of energy storage operations. Moreover, we emphasize that $\Gamma$ is inversely

proportional to injection rates, so the expressions derived herein are biased toward being applicable to larger energy storage operations.

## 4. Conclusions and Discussion

We have provided the vertically integrated model equations applicable for mass and energy balance in the context of injection from a single vertical well. These equations admit a self-similar scaling, and within this context we have derived analytical and approximate solutions utilizing the parameter ranges associated with subsurface energy storage.

The solutions derived herein compare well with numerically resolved simulations across a broad range of parameters. These parameters have been verified as relevant in the context of energy storage based on data from analogue industrial operations.

When considering aquifer energy storage in the context of intermittent renewable energy sources, approximate solutions such as those provided herein can form a valuable tool both for screening and ranking purposes, and also as proxy-solutions in system-level tools [see e.g., *Cody et al*., 2015; *Bachu*, 2015; *Celia et al*., 2011] for examples from $CO_2$ storage). On a theoretical level, such analytical solutions form the building blocks on which other physical processes can be preliminarily assessed (pressure buildup due to injection, thermally induced mechanical stresses, extent of altered geochemical conditions due to salinity and temperature change). On a practical level, these analytical solutions form the basis of understanding the realistic scales involved in the implementation of residential, commercial, or regional-scale energy storage concepts.

The present solutions consider the injection phase that is typified by strong advective drive, and thus it is reasonable to neglect effects such as thermal conduction in the rock. This is the phase where the spatial footprint of the storage operation is established. The full process of aquifer thermal storage necessarily includes both storage and recovery phases. The current work provides the initial conditions for the storage phase, wherein it is expected that both thermal conduction, as well as possibly thermal convection, may be of importance. Indeed, the adverse effects of thermal convection during the storage stage are one of the challenges to obtain efficiency for this technology [*Molz et al*., 1983].

## Notation

| | |
|---|---|
| $\zeta$ | Macroscopic fluid-fluid front (section 2.1) |
| $\rho$ | Density (equation (2.1)) |
| $\mu$ | Viscosity (section 2.1) |
| $h$ | Thickness (equation (2.3)) |
| $U$ | Integrated Darcy flux (equation (2.5)) |
| $r$ | Radial coordinate (equation (2.5)) |
| $k$ | Permeability (equation (2.5)) |
| $p$ | Fluid potential (equation (2.5)) |
| $\Delta_i$ | Difference across front $\zeta_i$ (equation (2.6)) |
| $g$ | Gravitational constant (equation (2.6)) |
| $\phi$ | Porosity (equation (2.7)) |
| $\gamma_T$ | Retardation coefficient (equation (2.8)) |
| $\kappa$ | Heat capacity (equation (2.9)) |
| $\Psi$ | Injection rate (equation (2.10)) |
| $\Gamma$ | Gravity number (equation (2.15)) |
| $\lambda$ | Viscosity ratio (equation (2.15)) |
| $\nu$ | Normalized density difference (equation (2.15)) |
| $\tau$ | Dimensionless time (equation (2.15)) |
| $\eta$ | Dimensionless distance (equation (2.15)) |
| $\chi$ | Self-similar space-time coordinate (equation (2.19)) |
| $\epsilon$ | Dimensionless excess mobility (equation (2.25)) |
| $H$ | Heaviside function (equation (2.31)) |

$a$ Inverse slope of fluid-fluid front $\zeta$ (equation (2.48))
$e$ Approximation error or difference (equation (3.1))

**Acknowledgments**
The author thanks Carina Bringedal (U. of Bergen), Florian Doster (Heriot-Watt U.), Sarah E. Gasda (Uni Research) and Bo Guo (Stanford U.) for discussions on this topic and comments on the manuscript. This work forms part of Norwegian Research Council projects 250223 and 215641. All data used for this study are properly cited and referred to in the reference list.

## References

Bachu, S. (2015), Review of CO2 storage efficiency in deep saline aquifers, *Int. J. Greenhouse Gas Control*, *40*, 188–202.
Bachu, S., and J. J. Carroll (2005), In-situ phase and thermodynamic properties of resident brine and acid gases (CO2 and H2S) injected in geological formations in western Canada: Demonstration of CO2 geological storage, Carbon Dioxide Capture for Storage, Deep Geologic Formations–Results from the CO2 Capture Project 2, 867–876.
Bachu, S., J. M. Nordbotten, and M. A. Celia (2005), Evaluation of the spread of acid-gas plumes injected in deep saline aquifers in western Canada as an analogue for CO2 injection into continental sedimentary basins, *Greenhouse Gas Control Technologies 7*, 479–487, doi:10.1016/b978-008044704-9/50049-5.
Barenblatt, G. I. (1996), *Scaling, Self-Similarity, and Intermediate Asymptotics*, Cambridge Univ. Press, Cambridge, U. K.
Bear, J. (1979), *Hydraulics of Groundwater*, McGraw-Hill, New York.
Celia, M. A. et al. (2011), Field-scale application of a semi-analytical model for estimation of CO2 and brine leakage along old wells. *Int. J. Greenhouse Gas Control*, *5*(2), 257–269.
Chen, Z., Y. Huan, and G. Ma (2006), *Computational Methods for Multiphase Flows in Porous Media*, Soc. of Ind. and Appl. Math, Philadelphia, Penn.
Cody, B., D. Bau, and A. Gonzales-Nicolas (2015), Stochastic injection strategy optimization for the preliminary assessment of candidate geological storage sites, *Hydrogeol. J.*, *23*(6), 1229–1245.
Court, B., et al. (2012), Applicability of vertical-equilibrium and sharp-interface assumptions in CO2 sequestration modeling, *Int. J. Greenhouse Gas Control*, *10*, 134–147.
Dudfield, P., and A. W. Woods (2012), On the periodic injection of fluid into, and its extraction from, a porous medium for seasonal heat storage, *J. Fluid Mech.*, *707*, 467–481.
Gasda, S. E., J. M. Nordbotten, and M. A. Celia (2012), Application of simplified models to CO2 migration and immobilization in large-scale geological systems, *Int. J. Greenhouse Gas Control*, *9*, 72–84.
Gasda, S. E., W. Gray, and H. K. Dahle (2014), *Vertically Integrated Models With Coupled Thermal Processes*, Elsevier, Catalina, Calif.
Guo, B., Z. Zheng, M. A. Celia, and H. Stone (2016), Axisymmetric flows from fluid injection into a confined porous medium, *Phys. Fluids*, *28*, 022107.
Hesse, M. A., F. M. Orr Jr., B. J. Cantwell, and Tchelepi (2007), Gravity currents in horizontal porous layers: Transition from early to late self-similarity, *J. Fluid Mech.*, *577*, 363–383.
Huppert, H., and A. W. Woods (1995), Gravity driven flows in porous layers, *J. Fluid Mech.*, *292*, 55–69.
Lake, L. (1989), *Enhanced Oil Recovery*, Prentice Hall, Englewood Cliffs, N. J.
LeFloch, P. G. (2002), *Hyperbolic Systems of Conservation Laws: The Theory of Classical and Non-Classical Shock Waves*, Birkhäuser, Basel, Switzerland.
LeVeque, R. J. (1992), *Numerical Methods for Conservation Laws*, Birkhäuser, Basel, Switzerland.
Molz, F. J., A. D. Parr, and P. F. Andersen (1981), Thermal energy storage in a confined aquifer: Second cycle, *Water Resour. Res.*, *17*, 641–645.
Molz, F. J., J. G. Melville, O. Güven, and A. D. Parr (1983), Aquifer thermal energy storage: An attempt to counter free thermal convection, *Water Resour. Res.*, *19*, 922–930.
Mykkeltvedt, T., and J. M. Nordbotten (2012), Estimating convective mixing rates from commercial-scale CO2 injection, *Environ. Earth Sci.*, *67*, 527–535.
Nayar, K. G., M. H. Sharqawy, L. D. Banchik, and J. H. Lienhard (2016), Thermophysical properties of seawater: A review and new correlations that include pressure dependence, *Desalination*, *390*, 1–24.
Nordbotten, J. M., and M. A. Celia (2006), Similarity solutions for fluid injection into confined aquifers, *J. Fluid Mech.*, *561*, 307–327.
Nordbotten, J. M., and M. A. Celia (2012), *Geological Storage of CO2: Modeling Approaches for Large-Scale Simulation*, John Wiley, Hoboken, N. J.
Nordbotten, J. M., and H. Dahle (2011), Impact of the capillary fringe in vertically integrated models for CO2 storage, *Water Resour. Res.*, *47*, W02537, doi:10.1029/2009WR008958.
Palmer, C. D., D. W. Blowes, E. O. Frind, and J. W. Molson (1992), Thermal energy storage in an unconfined aquifer 1. Field injection experiment, *Water Resour. Res.*, *28*, 2845–2856.
Perlinger, J. A., J. E. Almendinger, N. R. Urban, and S. J. Eisenreich (1987), Groundwater geochemistry of aquifer thermal energy storage: Long term test cycle, *Water Resour. Res.*, *23*, 2215–2226.
Rayward-Smith, W. J., and A. W. Woods (2011), On the propagation of non-isothermal gravity currents in an inclined porous layer, *J. Fluid Mech.*, *686*, 250–271.
Ueckert, M., R. Niessner, and T. Baumann (2016), *High Temperature Aquifer Storage*, Stanford Univ., Stanford, Calif.
Yortsos, Y. C. (1995), A theoretical analysis of vertical flow equilibrium, *Transp. Porous Media*, *18*, 107–129.